CANCER IMAGING

Intraoperative brain cancer detection with Raman spectroscopy in humans

Michael Jermyn,[1,2]* Kelvin Mok,[3]* Jeanne Mercier,[2] Joannie Desroches,[4] Julien Pichette,[2] Karl Saint-Arnaud,[2] Liane Bernstein,[2] Marie-Christine Guiot,[1,5] Kevin Petrecca,[1†‡] Frederic Leblond[2†‡]

Cancers are often impossible to visually distinguish from normal tissue. This is critical for brain cancer where residual invasive cancer cells frequently remain after surgery, leading to disease recurrence and a negative impact on overall survival. No preoperative or intraoperative technology exists to identify all cancer cells that have invaded normal brain. To address this problem, we developed a handheld contact Raman spectroscopy probe technique for live, local detection of cancer cells in the human brain. Using this probe intraoperatively, we were able to accurately differentiate normal brain from dense cancer and normal brain invaded by cancer cells, with a sensitivity of 93% and a specificity of 91%. This Raman-based probe enabled detection of the previously undetectable diffusely invasive brain cancer cells at cellular resolution in patients with grade 2 to 4 gliomas. This intraoperative technology may therefore be able to classify cell populations in real time, making it an ideal guide for surgical resection and decision-making.

INTRODUCTION

Diffusely invasive brain cancers, which include World Health Organization (WHO) grade 2 to 3 astrocytomas, grade 2 to 3 oligodendrogliomas, and grade 4 glioblastomas (GBMs), locally invade the normal brain, generating a decreasing gradient of cancer cells that extends from the main cancer mass into healthy tissue. These invasive cancer cells cannot be detected using the technologies that are currently used clinically. Visual detection of this cancer cell gradient using state-of-the-art bright-field neurosurgical microscopes is not possible. Magnetic resonance imaging (MRI), which serves as a preoperative, and occasionally intraoperative, navigational guide to surgery, is also unable to detect the full extent of cancer cell invasion and suffers from inaccuracies owing to brain shift (1–3). A newer fluorescence-guided approach to GBM surgery involves protoporphyrin IX (PpIX) and 5-aminolevulinic acid (5-ALA) but has shown limitations in its ability to detect grade 2 gliomas and the invasive cancer cells (4–8).

The inability to fully visualize invasive brain cancers results in subtotal surgical resections, and owing to the absence of effective adjuvant therapies such as radiotherapy and chemotherapy (for example, temozolomide and bevacizumab), incomplete resections negatively affect survival. Hence, more than 85% of GBM recurrences occur at the resection cavity margin (9). Retrospective and prospective outcome studies based on postoperative imaging have shown that the volume of residual cancer after surgery directly affects progression-free survival and overall survival for all grades of invasive gliomas and that complete resection—

based on MRI T2 signal (grades 2 and 3) or contrast enhancement (grade 4)—is a major factor in inhibiting recurrence and improving survival (10, 11). Conversely, unnecessary removal of brain tissue that does not contain cancer cells can lead to neurological deficits that affect quality of life, such as impaired cognition, memory, and vision (12, 13). Neurosurgery can thus benefit immensely from complementary techniques being introduced into the surgical workflow that can detect not only dense cancer but also invasive cancer cells around and beyond the tumor margins.

Advances have been made using a range of techniques to detect brain tumors with the goal of surpassing standard MRI and intraoperative visual assessment to improve the volume of tumor resection in brain surgery. Fluoro-ethyl-tyrosine positron emission tomography has been used preoperatively for surgical planning, showing greater sensitivity than MRI for cancer invasion, with 88% sensitivity for detecting grade 3 to 4 gliomas, but with 54% sensitivity for lower-grade gliomas (14). Modalities such as ultrasound (US) and optical coherence tomography (OCT) have been shown to provide structural information (large scale for US and microscopic scale for OCT) in real time (15, 16). US is unable to detect microscopic invasion, but intraoperative OCT has been able to distinguish high- versus low-density cancer in nine patients with high-grade gliomas (17). Intraoperative confocal microscopy has shown evidence for invasion detection using 5-ALA fluorescence in grade 1 to 2 gliomas on 10 patients (18). Although very promising, the statistical power of this study was limited, and the requirement for a contrast agent, as well as the need for surgeons to interpret complex, depth-resolved microscopy images during surgery, might deter clinical adoption.

Raman spectroscopy is a noninvasive modality that gives spectral tissue characteristics based on molecular signatures resulting from inelastic scattering of incident light. Inelastic scattering occurs when light interacts with matter, but its relative importance is diminished by competing phenomena, including elastic scattering and absorption. Hence, measuring the Raman effect in time frames compatible with the neurosurgical workflow is a challenge, requiring sophisticated optical technologies, including ultrastable monochromatic light sources, highly sensitive and high-speed spectroscopic sensors, as well as interference light filtering methods. Raman spectroscopy is used to observe low-frequency vibrational

modes in a system. Light from a near-infrared (NIR) laser interacts with those modes, resulting in the inelastic scattered photons being shifted in energy to values different than that of the excitation. This shift is measured in terms of the difference between the inverse of the excitation and detected wavelengths (units: cm^{-1}) and gives information that is specific to chemical bonds. The resulting spectra provide a fingerprint by which different molecular species can be identified and their relative concentration evaluated on the basis of the strength of different peaks. Biological tissues, including the brain, contains a large number of Raman-active molecules, resulting in spectroscopic measurements that are in effect a weighted sum of spectra from all molecular species contained within the interrogated tissue volume.

Haka *et al.* were among the first to investigate intraoperative in situ Raman spectroscopy for breast cancer margin detection (*19*). Other studies used the technique in vivo as a complement to endoscopy for human gastrointestinal applications (*20*), for the assessment of corneum hydration in dermatology applications (*21*), for the detection of precancerous cervical lesions with a sensitivity of 82% and a specificity of 92% (*22*), and for the diagnosis of bladder cancer with a sensitivity of 85% and specificity of 79% (*23*). Most Raman spectroscopy studies of brain cancer have been in rodent models and ex vivo human brain tissue (*24–28*). Toward surgical use, Ji *et al.* detected glioma invasion intraoperatively with Raman microscopy in a mouse model of human glioma, with spectral shift ranges higher than those probed in this study, therefore shedding light on different molecular features (*29*). Although these are impressive advances, Raman spectroscopy has yet to be tested in patients during surgical resection of brain cancer.

Here, we tested an intraoperative Raman-based probe technique to detect invasive brain cancer in situ in real time in patients. We demonstrate that Raman spectroscopy can accurately detect grade 2 to 4 gliomas in vivo during human brain cancer surgery, with the ability to distinguish cancer cell–invaded brain from normal brain, with sensitivity and specificity of >90%. This was accomplished using a handheld contact Raman spectroscopy probe illuminating a 0.5-mm-diameter tissue area with a depth sampling up to ~1 mm and a total acquisition time of 0.2 s. The technology was integrated into the neurosurgical workflow for live identification of invasive cancer with sensitivity beyond current imaging capabilities.

RESULTS

A handheld Raman spectroscopy probe

We developed a technique using a handheld contact fiber optic Raman spectroscopy probe (Emvision, LLC) capable of single-point submillimeter Raman signal detection (Fig. 1) with the goal of distinguishing brain cancer (glioma) from normal brain. The probe contained fiber optic cables connected to a NIR spectrum–stabilized laser emitting at 785 nm.

The probe was also connected to a high-speed and high-resolution charge-coupled device (CCD) spectroscopic detector. The laser and the imaging spectrometer were connected to a computer to visualize the Raman spectra in real time. The spectra covered a range of shifts from 381 to 1653 cm^{-1}, with a spectral resolution varying between 1.6 and 2.1 cm^{-1}.

During each tumor resection procedure, the probe measured the Raman signal at several points in the surgical cavity (Fig. 1B). The inelastic scattering (Raman) signal is several orders of magnitude smaller than that associated with Rayleigh scattering (elastic scattering). As a result, the main challenge was to detect and isolate the tissue inelastic scattering from the inelastic signal of the instrument itself and the elastic signal at the 785-nm excitation wavelength. To do this, the probe was fabricated using micrometer-scale in-line filters that were placed directly at the tip of the optical fibers (Fig. 1A). A narrow 785 nm–centered band-pass filter was used at the tip of the excitation fiber, and a long-pass filter was used to further attenuate the elastically scattered light from the excitation laser. The total acquisition time was 0.2 s, which
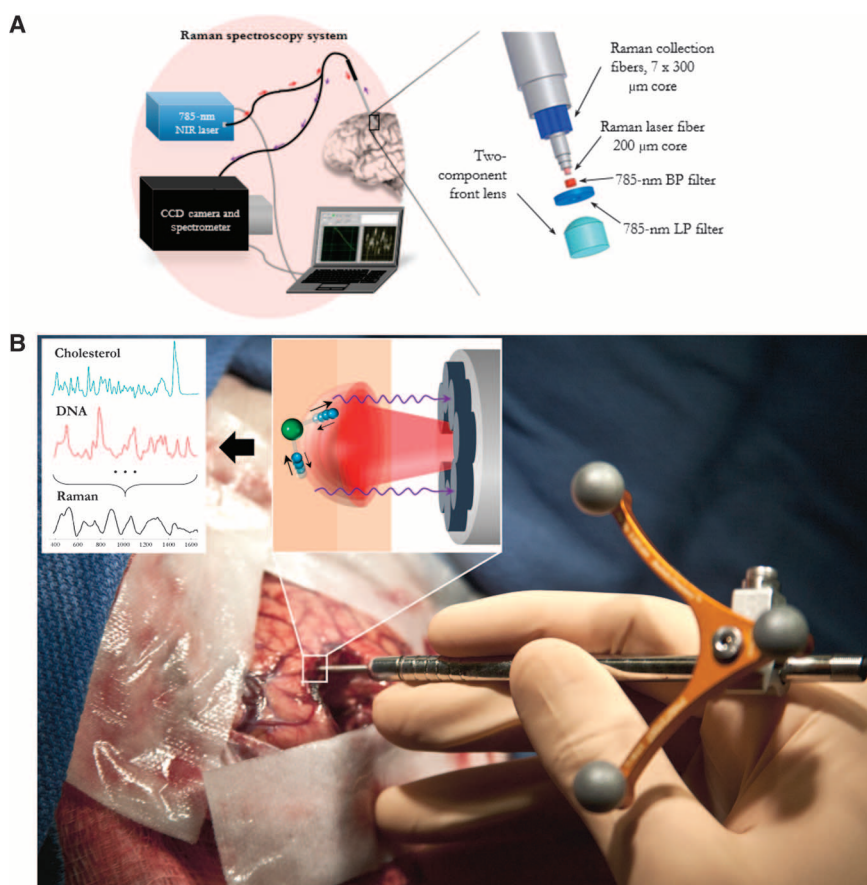
Fig. 1. The handheld contact fiber optic probe for Raman spectroscopy. (**A**) Experimental setup diagram with the 785-nm NIR laser and the high-resolution CCD spectroscopic detector used with the Raman fiber optic probe. The core material was fused silica. BP, band-pass; LP, long-pass. (**B**) The probe (Emvision, LLC) was used to interrogate brain tissue during surgery. A schematic diagram illustrates the excitation of different molecular species, such as cholesterol and DNA, to produce the Raman spectra of cancer versus normal brain tissue. The spectral differences occur owing to the vibrational modes of various molecular species. A simple molecular vibrational mode is conceptually depicted (individual atoms in blue and green) interacting with the laser light (in red) to produce Raman scattering (in purple).

corresponded to three acquisitions of Raman spectra plus a background measurement (no laser excitation). The circular laser spot size of the probe had a diameter of 0.5 mm (area of 0.2 mm^2).

Light transport simulations in tissue were performed (fig. S1) using Mesh-based Monte Carlo (30, 31), demonstrating that the sampling depth of the probe associated with 95% of the Raman signal comes from the first ~1 mm beneath the surface. A signal-to-noise ratio of 15.8 was calculated for the system [as in (20)] as the ratio of the Raman peak size versus the noise, with noise defined as the difference between the maximum and minimum intensities in the baseline of the Raman spectra (20). The acetaminophen spectrum was used as a standard for this calculation, with peaks in the spectrum chosen closest in size to those seen in the spectra of brain tissue.

In vivo imaging protocol

A total of 161 measurements were collected (Table 1) using the fiber optic probe (Fig. 1) in 17 patients with WHO grade 2 to 4 gliomas undergoing brain cancer surgery. Here, emphasis was placed on interrogating brain regions both within the MRI-defined dense cancer and outside (up to 1.5 cm) of the T1-gadolinium enhancing and T2-weighted hyperintense regions in grade 2 to 4 gliomas. Although state-of-the-art neuronavigation techniques are used in this study, MRI information was used only qualitatively for visualization and for estimating the location of each Raman measurement on the preoperative images (that is, the position of the crosshairs in Fig. 2 and figs. S2 and S4). As a result, this information (and the inherent inaccuracies associated with the neuronavigation tracking system) had no impact on our ability to spatially relate the biopsied samples and the probe measurement locations.

Each probe interrogation site was biopsied and archived for postsurgery, blinded, histopathological analysis. At each of the 161 inter-

Table 1. Patient demographics and histological diagnosis. Diagnoses were made according to the WHO, on the basis of the consensus of pathologists and international experts, providing definition for brain tumors in cancer research (47). For the "Other" classification, only normal brain samples were used from the indicated patients; no samples with cancer cells present were acquired.

		n patients	n samples
Age (years), median (range)	53 (30–89)		
WHO grade	Grade 2	4	35
	Astrocytoma	3	26
	Oligodendroglioma	1	9
	Grade 3	3	29
	Astrocytoma	1	10
	Oligodendroglioma	1	10
	Oligoastrocytoma	1	9
	Grade 4 (GBM)	8	68
	Other: metastatic	2	29
Tissue type	Normal brain		66
	Dense cancer		39
	Invasive cancer cells		56
Total		17	161

rogation points, the surgeon also commented, on the basis of tissue appearance (visual assessment through the surgical microscope) and navigation guidance data (preoperative MRI spatially registered with the surgical field), whether the interrogated area likely corresponded to normal brain (negative for cancer cells) or cancer.

Blinded neuropathological analysis of each biopsy sample was performed using hematoxylin and eosin (H&E) staining. For samples arising from tumors containing the isocitrate dehydrogenase 1 (IDH1) (R132H) mutation, immunohistochemistry using an anti-IDH1 (R132H)–specific antibody was used as a complementary technique to identify cancer cells. On the basis of these neuropathological analyses, each sample was classified as either normal brain (no cancer cells present), normal brain infiltrated with invasive cancer cells (≤90% cancer cells present), or dense cancer (>90% cancer cells present) (Table 1). For 77 of the 161 biopsy samples collected, the background could clearly be identified by the pathologist as either white matter or gray matter ($n = 36$ samples in gray matter, $n = 41$ samples in white matter). Figure S3 shows the average Raman spectrum of all samples with gray matter and the average spectrum of all samples with white matter. Some samples consisted of part white matter and part gray matter and so were not included in fig. S3.

Figure 2A and movie S1 show the preoperative MRI in 3D of a patient with a grade 2 glioma, with the Raman spectroscopy measurement locations identified as blue (normal) and yellow (cancer) dots. For three of the measurement locations, in dense cancer, invasive cancer, and normal brain, the 2D MRI slices are provided with corresponding pathology images, as well as the Raman spectra obtained at these measurement locations (Fig. 2B). Sample Raman spectra, preoperative MRI, and pathology images are also provided for a patient with a grade 3 glioma (fig. S2) and a patient with a grade 4 glioma (Fig. 2C).

Intraoperative Raman spectroscopy for real-time detection of brain cancer

We found that the measured average Raman spectra for all normal brain and cancer (either normal brain infiltrated with invasive cancer cells or dense cancer) tissue samples showed differences in the molecular signature of the specimens (Fig. 3A) consistent with past work on ex vivo brain tissue samples (26, 27, 32). The specimens with cancer cells showed differences in the lipid bands at 700 and 1142 cm^{-1} compared to normal brain, corresponding to cholesterol and phospholipids (26). The presence of cancer cells also showed an increase of the bands from 1540 to 1645 cm^{-1}, corresponding to a higher nucleic acid content than normal brain tissue, as observed previously for GBM (27). Cancer tissue also showed an increase in the 1005 cm^{-1} band, associated with the breathing mode of phenylalanine in proteins (26).

To utilize all of the spectral information available in the Raman signals we acquired, we used the boosted trees machine learning method to analyze the spectra and determine classification criteria, allowing samples from all cancer tissue categories to be separated from samples corresponding to normal brain (33). Using this technique, we were able to distinguish normal brain from tissue with the presence of cancer cells (including both invasive and dense cancers) with an accuracy of 92%, sensitivity of 93%, and specificity of 91% (Table 2, Eqs. 1 to 3). For the classification of normal brain from all samples with cancer cells (from all grades of glioma and including both dense and invasive cancers), we obtained a ROC curve with AUC of 0.96 (Fig. 3B). In comparison, the sample labels (either normal brain or cancer) given by the surgeon after visual inspection using a bright-field microscope and MR guidance produced an accuracy of 73%, sensitivity of 67%, and specificity of 86%.

Fig. 2. Raman spectroscopy measurements colocated on preoperative MRI–grade 2 and 4 gliomas. (**A**) Three-dimensional (3D) volume rendering of a preoperative T2-weighted MRI overlaid with the segmentation of a grade 2 astrocytoma in red. MRI information is used only qualitatively for visualization, not for spatial registration between histology and the location of the Raman probe measurement. Regions associated with dots were interrogated by Raman spectroscopy and were histologically analyzed. Yellow sample locations indicate the presence of cancer cells; blue locations were negative for cancer cells. Representative samples for each tissue type are indicated by P1, P2, and P3. (**B**) Corresponding pathology images for regions P1 to P3 in (A). P1, P2, and P3 are dense cancer, invasive cancer, and normal brain, respectively. T2-weighted MRI images are accompanied by histopathology. The acquired Raman spectra are shown below for P1 to P3. (**C**) In a different patient than (A) and (B) with grade 4 GBM, sample locations for dense cancer, invasive cancer, and normal brain are shown on a T1-weighted MRI. Histopathology images are below. MRI and histopathology images are shown for a patient with grade 3 anaplastic astrocytoma in fig. S2. The acquired Raman spectra are shown below for P1 to P3. a.u., arbitrary unit.
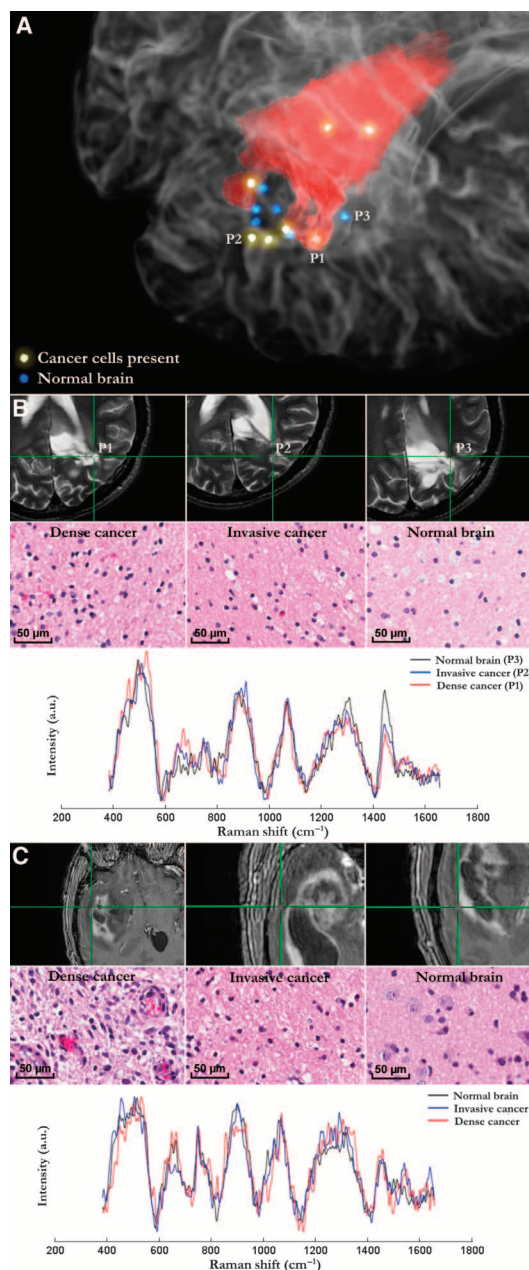
As reported in Table 2, using Raman spectra, we obtained classification accuracies of 90% or more between normal brain and all tumor grades, as well as between normal brain and either dense cancer or the invasive cancer cell categories. We were further able to distinguish WHO grade 2 from grade 3 and 4 gliomas in the dense cancer population with 82% accuracy based on Raman spectroscopy. However, we were unable (accuracy, sensitivity, and specificity lower than 60%) to distinguish between different WHO grades in the normal brain infiltrated with invasive cancer cells or between grade 3 and 4 gliomas.

Cancer cell threshold

To estimate the cancer cell density threshold that can be detected by the Raman spectroscopy technique, we performed histological cell counting for a subset ($n = 14$) of the 56 samples designated as normal brain infiltrated by invasive cancer cells (Table 2). The 14 samples were selected because they were determined by the pathologist to correspond (on the basis of the analysis of all H&E images) to those with the lowest density of cancer cells. Of these 14 samples, 5 were false negatives by Raman spectroscopy classification; that is, the spectral classification was normal brain, but cancer cells were found in the corresponding H&E-stained biopsy samples. The remaining nine samples were true positive by Raman spectroscopy classification.

For each of the 14 samples, multiple regions of interest (each 250 μm × 250 μm) were delineated by the neuropathologist on the digitally scanned H&E images. The total number of normal and cancer cells was determined, and the average over the multiple regions of interest was established for cell count per area. The cancer cell counting was validated with mutant IDH1 (R132H) immunohistochemistry. The cancer cell count per area, the total cell count per area, and the cancer cell burden (cancer cell count divided by the total cell count) determined by H&E are reported in Table 3. All false-negative Raman spectroscopy classifications corresponded to <15% cancer cell burden, and all samples having tested positive for cancer (based on spectroscopy) had >15% cancer cell burden. In absolute terms, the Raman probe was able to detect the presence of as few as 17 human cancer cells/0.0625 mm^2.

DISCUSSION

The prognosis for patients with grade 2 gliomas is better than that of grade 3 and 4 gliomas because these cancers, in general, grow more slowly, have a more favorable response to adjuvant radiotherapy and chemotherapy, and most often occur in younger patients with excellent performance status who are able to tolerate the adjuvant therapies. Invariably, grade 2 cancers progress to grades 3 and 4. This understanding of the natural history of grade 2 gliomas has led to an interest in earlier and more aggressive treatments, which include surgical cytoreduction. Retrospective data suggest that maximal surgical resection provides a major survival benefit for patients with grade 2 gliomas, in some cases up to additional decades (34–38). There is similarly strong evidence showing that the extent of tumor resection for grade 3 and 4 gliomas also affects survival (10, 11, 39, 40). As a result, the main goal of glioma surgery is to minimize the volume of residual cancer remaining after surgery to prolong survival and alleviate symptoms while minimizing
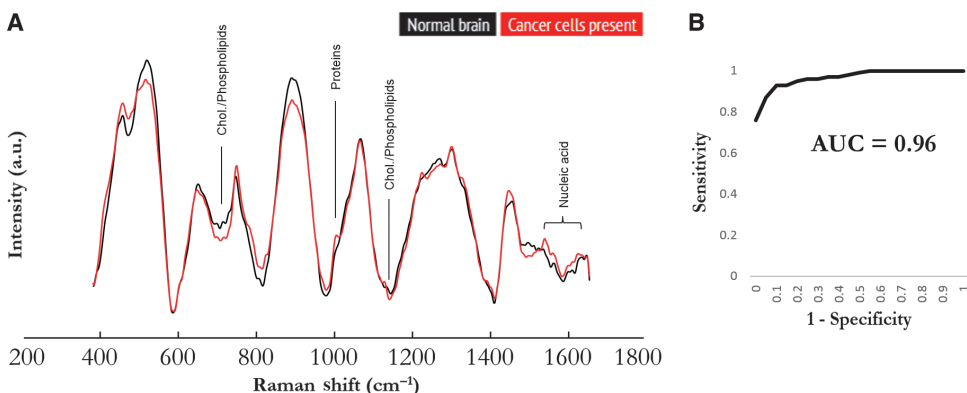
Fig. 3. Raman spectra for discrimination of cancer tissue. (**A**) Average Raman spectra of in vivo measurements for normal brain (all 66 spectra averaged) and tissue containing glioma cancer cells (all 95 spectra averaged). The corresponding molecular contributors are identified for the most significant differences between the spectra for normal and cancer tissues. Chol., cholesterol. (**B**) Receiver operating characteristic (ROC) curve analysis of in vivo detection of glioma based on Raman spectroscopy. This was generated using the boosted trees classification method. AUC, area under the curve.

Table 2. Comparison of tissue classification based on Raman spectroscopy with histopathology, categorized by grade of glioma or tissue type. Accuracy, sensitivity, and specificity results are listed. The "Clinical practice" category indicates the performance based on the neurosurgeon's assessment (from visual inspection and MRI). All "normal brain" measurements (n = 66 tissue samples; Table 1) were used in calculating specificity, because it is not related to grade or type. See Table 1 for the number of samples per category. A two-sided normal-based 95% confidence interval (CI) of smaller than ±5% was obtained for each category.

	Accuracy (%)	Sensitivity (%)	Specificity (%)
WHO grade			
2	91	91	91
3	91	89	91
4	93	94	91
Tissue type			
Dense cancer	93	97	91
Invasive cancer cells	90	89	91
Total	92	93	91
Clinical practice	73	67	86

the risk for neurological injury associated with the unnecessary resection of normal tissue.

Attaining this goal is challenging because grade 2 to 4 gliomas are highly invasive, which is manifested by the fact that these cancers are not restricted to areas of MRI contrast uptake and/or T2 hyperintensity. Gliomas invade beyond the visible MRI borders, with distant cancer cell invasion not being grossly detectable during surgery using standard-of-care technologies (41). For example, it is because grade 2 to 4 gliomas are not associated with a defined biological interface between cancerous and normal tissue that radiotherapy protocols include radiation to fields that are typically up to 2 cm beyond the total MRI signal abnormality.

We show here that in vivo Raman spectroscopy is capable of accurate, sensitive, and specific tissue classification of invasive brain cancers for grade 2 to 4 gliomas. This is achieved using a small-footprint handheld fiber optic probe technique designed for rapid (<0.2 s) intraoperative inelastic scattering spectroscopic measurements. The resulting spectra capture the biological information associated with a multitude of molecular components within a tissue surface diameter of 0.5 mm and a depth no larger than ~1 mm. This level of tissue sampling is appropriate for surgery because it is consistent with the level of precision neurosurgeons can reach using state-of-the-art neurosurgical microscopes and tissue dissection techniques. The handheld Raman probe is small and operates in real time, making it convenient during brain cancer resection with minimal disruption to the neurosurgical workflow (movie S2). This makes the probe useful during surgery, because it can rapidly detect cancer at a point of interest without the need for biopsy and frozen neuropathology assessment, which can disrupt the surgical workflow when performed several times during a procedure. Contrary to other pathologies (for example, skin cancer, breast cancer, mouth and throat cancer, and colon cancer), the standard of care in neurosurgical oncology does not include multiple tissue biopsies around the tumor bulk to identify clean margins.

Specifically, we have shown that Raman spectroscopy is highly sensitive and specific to brain cancer tissue. With this technology, we were able to distinguish normal brain from cancer (normal brain infiltrated with invasive cancer cells and dense cancer) with an accuracy of at least 90% for grade 2 to 4 gliomas. We have also demonstrated that the probe can distinguish normal brain from normal brain infiltrated with invasive cancer cells with an accuracy of 90%. We have further shown the estimated cellular resolution of the Raman probe, with detection of as few as 17 cancer cells/0.0625 mm^2. These findings are important because minimizing the volume of residual cancer has a measurable impact on patient survival. Molecular fingerprinting based on Raman-active molecules may also shed new light on our understanding of human brain cancer biology. Here, however, we are reporting on an automated tissue classification technique that is using the full spectrum—rather than separation based on the identification of a few distinguishing bands—to use all of the molecular information to provide a diagnostic measure. Detection at this cellular resolution level goes beyond the current standard-of-care capabilities of visual inspection through a bright-field neurosurgical microscope, intraoperative MRI, and 5-ALA–PpIX imaging, which primarily reveal bulk tumor (dense cancer) (4, 5, 14).

Although the current study was not designed to guide surgical resection (the Raman spectroscopy results were blinded to the surgeon), in the future, optical diagnostics information could be provided in real time to the surgeon because signal computations, including preprocessing and tissue classification, occur in <1 s. The ability of the instrument

Table 3. Estimating the cancer cell resolution capability of the hand-held Raman spectroscopy probe. The total number of cells (both normal and cancer cells) and the number of cancer cells were quantified in 14 different patient samples of normal brain invaded with cancer cells. Cells were counted in multiple areas of 250 μm × 250 μm (0.0625 mm^2), and the average was determined. Samples with an asterisk (*) are those for which cancer cell density was quantified using both H&E and IDH1 (R132H) immunohisto-chemistry (IHC). These samples have the cell count values obtained using IHC in parentheses. Note that 1 of the 14 samples consisted of both gray matter and white matter explaining why cell counting information is presented for both in that case. Each of the other samples was either all gray matter or all white matter.

Biopsy sample	Raman classification (positive or negative for cancer cells)	Total cell count per area	Cancer cell count per area	Cancer cell burden (%)
1	Positive	95	17	18
2	Positive*	104 (IHC: 70)	30 (IHC: 19)	29 (IHC: 27)
3	Positive	78	55	71
4	Positive	85	58	69
5	Positive	113	98	87
6	Positive	92	83	90
7	Positive	65	52	80
8	Positive*	76 (IHC: 74)	65 (IHC: 59)	85 (IHC: 80)
9	Positive	49 (gray matter) 74 (white matter)	25 (gray matter) 60 (white matter)	51 (gray matter) 81 (white matter)
10	Negative	25	2	8
11	Negative*	35 (IHC: 51)	4 (IHC: 6)	11 (IHC: 12)
12	Negative	43	5	12
13	Negative	56	6	11
14	Negative*	136 (IHC: 118)	17 (IHC: 10)	13 (IHC: 9)

to detect even a low level of invasive cancer may prove to be important in glioma surgery.

Raman spectroscopy does not require the use of an exogenous compound to provide optical contrast, simplifying clinical use. The utility of this technique is in providing rapid cancer detection for a specific location of interest for the surgeon, particularly in white matter tracts with invasion. Tissue removal from such areas occurs using microdissection techniques, often with functional monitoring, making the probe an appropriate tool for intraoperative neurosurgical guidance. Despite its high cancer detection accuracy and ease of use, the instrument is intrinsically limited by its relatively restricted field of view (when compared to that of a neurosurgical microscope) and the requirement for an extra instrument to be introduced into the surgical workflow. Thus, there is potential for using complementary imaging techniques for guidance during glioma surgery. 5-ALA–PpIX fluorescence-guided surgery allows for wide-field identification of bulk cancer in GBMs with the same field of view as neurosurgical microscopes (4, 8). Fluorescence imaging can complement Raman spectroscopy for single-point detection of the peripherally invasive non-enhancing locations. A major advantage of the probe is to detect invasive cancer within normal brain that may not be grossly enhancing with 5-ALA–PpIX and MRI. Although this would also require the introduction of a handheld probe, the structural information obtained using OCT could be used to identify disrupted myelin fibers as a surrogate marker of possible locations of glioma invasion along white matter tracts, to be further interrogated by Raman spectroscopy to verify the presence of cancer tissue.

The ability of Raman spectroscopy to detect invasive brain cancer in all grades of glioma fills a needed role in neurosurgical guidance. Only relatively recently has photodetection technology been made available that is capable of detecting the effect in a fraction of a second with negligible disruption of the surgical workflow. Furthermore, isolation of the tissue-specific signature requires sophisticated micrometer-scale light filtering components. Technological advances in instrumentation have allowed Raman spectroscopy to be used in a clinical setting. A limitation associated with the routine clinical use of Raman spectroscopy (as with other optical techniques, such as fluorescence and OCT) is that it requires a proper illumination setup to limit extraneous light sources in the measured signal. Optical filters and other engineering solutions (for example, automated ambient light source adjustments) can be used to limit the effect of these sources when designing future operating rooms optimized for the detection of low-intensity spectroscopic signals. This work presents a technique for rapid in vivo intraoperative identification of invasive brain cancer with >90% accuracy and sets the stage for a clinical trial to evaluate its effectiveness for surgical guidance and early glioma detection with standard-of-care technology.

MATERIALS AND METHODS

Study design
The objective of this study was to evaluate the potential of Raman spectroscopy to distinguish brain cancer (either normal brain invaded by cancer cells or dense cancer) from normal brain in grade 2 to 4 gliomas. This study investigated the use of single-point Raman spectroscopy for intraoperative use in adult neurosurgical patients ($n = 17$) at the Montreal Neurological Institute and Hospital with grade 2 to 4 gliomas. Consecutive patients with suspected gliomas were included. Informed consent was obtained from each patient and monitored by the Montreal Neurological Institute Ethics Review Board. Patients received a complete preoperative neurological examination and standard clinical imaging. Sample sizes are in Table 1 and were chosen to give 95% CIs of less than ±5% for the classification accuracy in each category (tissue type or grade of glioma). The surgeon was blinded to any information about the acquired Raman spectra during the resection procedure. The pathologist was blinded to any information about the Raman spectra before performing the histological analyses. Samples were excluded from analysis if they were entirely necrotic, if saturation of the CCD occurred, if they were determined by the pathologist to have substantial heterogeneity in cancer cell density (part of the sample with the presence of cancer cells and part with no cancer cells), or in the presence of noticeable signal artifacts from the Medtronic system or operating room lights.

Handheld contact Raman spectroscopy probe
The probe contained fiber optic cables (Emvision, LLC) connected to a NIR spectrum–stabilized laser emitting at 785 nm (Innovative Photonic Solutions). The probe was connected to a high-speed and high-resolution

CCD spectroscopic detector (Andor Technology). The laser and the imaging spectrometer were connected to a PC computer with a LabVIEW interface. The spectra covered a range of spectral shifts from 381 to 1653 cm^{-1}, with a spectral resolution varying between 1.6 and 2.1 cm^{-1} across the spectral domain.

All data processing was performed in MATLAB (MathWorks Inc.). The probe had a navigation attachment (Medtronic SureTrak) for spatial registration with the Medtronic StealthStation system, allowing for intraoperative MR guidance of measurement and tissue sample collection locations. To correct for brain shift during surgery and thus maximize probe positioning accuracy, we recorded several landmarks using preoperative MRI before taking measurements. These fiducial markers were compared with a reconstructed cortical surface (from segmented preoperative MR images) and used to estimate brain shift.

Intraoperative optical data acquisition and tissue sample collection procedures

Before the surgical procedure, the probe and connecting equipment are sterilized using the STERRAD system. The CCD was cooled to −40°C, and all extraneous lights in the operating room were turned off, with only two operating room lights at low power left active (Dr. Mach, model 380). During surgery, the neurosurgeon used a white light from the OPMI Pentero surgical microscope system (Zeiss). Suitable measurement locations were selected by the neurosurgeon using MR guidance from the navigation system. For this study, the goal was to select normal brain, dense cancer, and normal brain infiltrated with invasive cancer cells at various locations in and around the tumor area detected on the MR images. Samples were acquired in both gray matter and white matter.

Before probe measurements, the surgeon minimized blood in the area being sampled. A measurement was then made with the Raman spectroscopy probe in direct contact with the brain tissue, with the bright-field microscope's white light turned off temporarily. The measurement location was marked on the MRI using the Medtronic StealthStation (crosshairs in Fig. 2 and fig. S2). Because the latter uses optical tracking for navigation with a strong NIR signal, the tracking mount was temporarily pointed away from the patient while the Raman measurement was taken. A reference measurement was first taken with the laser off with an integration time of 0.05 s. Then, three Raman measurements were taken with an integration time of 0.05 s each. The total measurement time was 0.2 s. Every time a Raman measurement was made, the probe was gently placed in contact with brain tissue to ensure that no air gap existed between probe and tissue surface. This invariably left (on white matter or any other brain tissue type) a temporary circular demarcation on the tissue surface, which was used by the surgeon as target location where a tissue biopsy sample was collected immediately after the measurement. The sample—on average with a size of ~0.5 mm × ~0.5 mm and a depth (from the surface) of ~3 mm—was then removed from the patient and preserved in formalin, to be archived and analyzed by a neuropathologist at a later date.

Laser power was adjusted before each procedure to account for differences in ambient light and intrinsic tissue fluorescence to avoid saturating the CCD. The laser power output as measured at the tip of the Raman probe ranges from 37 to 64 mW. The neurosurgeon's impression for each sample was also recorded (that is, whether the sample was thought to correspond to cancer or normal brain) to allow for comparison with the classification efficacy associated with the Raman probe.

Neuropathology assessment

All pathology analyses were performed by a neuropathologist specialized in neuro-oncology (M.-C.G.). On the basis of standard clinical practice, atypical cells were identified on H&E-stained sections on the basis of their morphological features, including nuclear atypia and nuclear polymorphism. As part of the standard neuropathological analysis, each tumor is also tested for the IDH1 (R132H) mutation, a known glioma marker (42). On the subset of tumors positive for the mutation, IDH1 (R132H) immunohistochemistry analyses were also conducted. Cell counting (total cell count per area, cancer cell count per area, and cancer cell burden) was done for 14 samples on the basis of H&E stain images. Further, cell counting based on immunohistochemistry was also done on $n = 4$ invasive cancer samples from three different patients (two of the four samples belonged to the same patient) having tested positive for the IDH1 (R132H) mutation. For those samples, the normal and cancer cell (positively stained cells) count per unit area was computed, and the cancer cell burden was evaluated. The immunohistochemistry for the IDH1 R132H antibody clone H09 (Dianova) was performed on an automatic immunostainer BenchMark XT (Ventana), using a pretreatment with Cell Conditioning 1 (CC1) and the XT OptiView DAB kit. The antibody was diluted 1:100. Immunostains were not performed on the next serial section from the H&E; therefore, although the absolute number of cells might differ, the cancer cell burden is comparable.

This study was designed to minimize spatial inconsistencies between the biopsied tissue and the actual volume sampled with light by the Raman. The average biopsy sample surface area was the same as the surface area sampled with the probe (0.5 mm × 0.5 mm). Biopsy samples were taken superficially using standard microdissection surgical instruments.

Statistical analysis and tissue classification

The background reference measurement was subtracted from each corresponding spectrum to account for ambient light sources. The spectra were then preprocessed to normalize for laser power and to remove intrinsic tissue fluorescence via an iterative fourth-order polynomial fit method (43). A variety of classification algorithms have been used to analyze Raman spectra in previous studies, including support vector machines, linear discriminant analysis, and artificial neural networks (27, 32, 44). The boosted trees method was chosen for analysis based on comparisons of learning algorithms, with superior performance overall (45, 46). It is robust to noise in the training data as well as the test data, an important quality given the rarity of the Raman effect relative to background signal. Furthermore, the algorithm does not make assumptions about feature independence and performs consistently even for a large amount of spectral information.

Boosted trees operates by constructing an ensemble of decision trees from training data. Each decision tree has a classification rule and operates on the residual of the classification determined by the previous decision tree (33). Classification was applied using a leave-one-out cross-validation approach. Cross-validation analysis was also used to determine the optimal number of decision trees for use in the classification, resulting in the use of eight decision trees. This was to avoid overfitting the data while maintaining sufficient complexity for proper classification. Statistical analysis on classification accuracy was performed using two-sided normal-based 95% CIs. Classification accuracy, sensitivity, and specificity were determined by Eqs. 1 to 3 on the basis of cancer detection outcomes of

true positive (TP), true negative (TN), false positive (FP), and false negative (FN):

$$\text{Accuracy} = \frac{\text{TP} + \text{TN}}{\text{TP} + \text{TN} + \text{FP} + \text{FN}} \quad (1)$$

$$\text{Sensitivity} = \frac{\text{TP}}{\text{TP} + \text{FN}} \quad (2)$$

$$\text{Specificity} = \frac{\text{TN}}{\text{FP} + \text{TN}} \quad (3)$$

SUPPLEMENTARY MATERIALS

www.sciencetranslationalmedicine.org/cgi/content/full/7/274/274ra19/DC1
Fig. S1. Sampling volume based on light transport modeling.
Fig. S2. Raman spectroscopy measurements colocated on preoperative MRI–grade 3 glioma.
Fig. S3. Raman spectra for gray matter and white matter.
Fig. S4. Preoperative MRI navigation location for the patient in movie S2.
Movie S1. 3D brain rendering with Raman spectroscopy cancer detection.
Movie S2. Use of the handheld probe in vivo with biopsy sample.

REFERENCES AND NOTES

1. M. H. T. Reinges, H.-H. Nguyen, T. Krings, B.-O. Hütter, V. Rohde, J. M. Gilsbach, Course of brain shift during microsurgical resection of supratentorial cerebral lesions: Limits of conventional neuronavigation. *Acta Neurochir.* **146**, 369–377 (2004).
2. K. A. Ganser, H. Dickhaus, A. Staubert, M. M. Bonsanto, C. R. Wirtz, V. M. Tronnier, S. Kunze, Quantification of brain shift effects in MRI images. *Biomed. Tech.* Suppl. 42, 247–248 (1997).
3. D. L. Hill, C. R. Maurer Jr., R. J. Maciunas, J. A. Barwise, J. M. Fitzpatrick, M. Y. Wang, Measurement of intraoperative brain surface deformation under a craniotomy. *Neurosurgery* **43**, 514–526 (1998).
4. W. Stummer, A. Novotny, H. Stepp, C. Goetz, K. Bise, H. J. Reulen. Fluorescence-guided resection of glioblastoma multiforme by using 5-aminolevulinic acid-induced porphyrins: A prospective study in 52 consecutive patients, *J. Neurosurg.* **93**, 1003–1013 (2000).
5. A. Nabavi, H. Thurm, B. Zountsas, T. Pietsch, H. Lanfermann, U. Pichlmeier, M. Mehdorn; 5-ALA Recurrent Glioma Study Group, Five-aminolevulinic acid for fluorescence-guided resection of recurrent malignant gliomas: A phase II study. *Neurosurgery* **65**, 1070–1076 (2009).
6. K. Roessler, A. Becherer, M. Donat, M. Cejna, I. Zachenhofer, Intraoperative tissue fluorescence using 5-aminolevolinic acid (5-ALA) is more sensitive than contrast MRI or amino acid positron emission tomography (^{18}F-FET PET) in glioblastoma surgery. *Neurol. Res.* **34**, 314–317 (2012).
7. P. A. Valdés, F. Leblond, A. Kim, B. T. Harris, B. C. Wilson, X. Fan, T. D. Tosteson, A. Hartov, S. Ji, K. Erkmen, N. E. Simmons, K. D. Paulsen, D. W. Roberts, Quantitative fluorescence in intracranial tumor: Implications for ALA-induced PpIX as an intraoperative biomarker. *J. Neurosurg.* **115**, 11–17 (2011).
8. P. A. Valdés, F. Leblond, V. L. Jacobs, B. C. Wilson, K. D. Paulsen, D. W. Roberts, Quantitative, spectrally-resolved intraoperative fluorescence imaging. *Sci. Rep.* **2**, 798 (2012).
9. K. Petrecca, M.-C. Guiot, V. Panet-Raymond, L. Souhami, Failure pattern following complete resection plus radiotherapy and temozolomide is at the resection margin in patients with glioblastoma. *J. Neurooncol.* **111**, 19–23 (2013).
10. N. Sanai, M. S. Berger, Glioma extent of resection and its impact on patient outcome. *Neurosurgery* **62**, 753–764 (2008).
11. M. Lacroix, D. Abi-Said, D. R. Fourney, Z. L. Gokaslan, W. Shi, F. DeMonte, F. F. Lang, I. E. McCutcheon, S. J. Hassenbusch, E. Holland, K. Hess, C. Michael, D. Miller, R. Sawaya, A multivariate analysis of 416 patients with glioblastoma multiforme: Prognosis, extent of resection, and survival. *J. Neurosurg.* **95**, 190–198 (2001).
12. W. Stummer, J.-C. Tonn, H. M. Mehdorn, U. Nestler, K. Franz, C. Goetz, A. Bink, U. Pichlmeier, ALA-Glioma Study Group, Counterbalancing risks and gains from extended resections in malignant glioma surgery: A supplemental analysis from the randomized 5-aminolevulinic acid glioma resection study. Clinical article. *J. Neurosurg.* **114**, 613–623 (2011).
13. I.-F. Talos, K. H. Zou, L. Ohno-Machado, J. G. Bhagwat, R. Kikinis, P. M. Black, F. A. Jolesz, Supratentorial low-grade glioma resectability: Statistical predictive analysis based on anatomic MR features and tumor characteristics. *Radiology* **239**, 506–513 (2006).
14. C. Ewelt, F. W. Floeth, J. Felsberg, H. J. Steiger, M. Sabel, K.-J. Langen, G. Stoffels, W. Stummer, Finding the anaplastic focus in diffuse gliomas: The value of Gd-DTPA enhanced MRI, FET-PET, and intraoperative, ALA-derived tissue fluorescence. *Clin. Neurol. Neurosurg.* **113**, 541–547 (2011).
15. H. J. Böhringer, D. Boller, J. Leppert, U. Knopp, E. Lankenau, E. Reusche, G. Hüttmann, A. Giese, Time-domain and spectral-domain optical coherence tomography in the analysis of brain tumor tissue. *Lasers Surg. Med.* **38**, 588–597 (2006).
16. J. Regelsberger, F. Lohmann, K. Helmke, M. Westphal, Ultrasound-guided surgery of deep seated brain lesions, *Eur. J. Ultrasound* **12**, 115–121 (2000).
17. H. J. Böhringer, E. Lankenau, F. Stellmacher, E. Reusche, G. Hüttmann, A. Giese, Imaging of human brain tumor tissue by near-infrared laser coherence tomography. *Acta Neurochir.* **151**, 507–517 (2009).
18. N. Sanai, L. A. Snyder, N. J. Honea, S. W. Coons, J. M. Eschbacher, K. A. Smith, R. F. Spetzler, Intraoperative confocal microscopy in the visualization of 5-aminolevulinic acid fluorescence in low-grade gliomas. *J. Neurosurg.* **115**, 740–748 (2011).
19. A. S. Haka, Z. Volynskaya, J. A. Gardecki, J. Nazemi, J. Lyons, D. Hicks, M. Fitzmaurice, R. R. Dasari, J. P. Crowe, M. S. Feld, In vivo margin assessment during partial mastectomy breast surgery using Raman spectroscopy. *Cancer Res.* **66**, 3317–3322 (2006).
20. M. G. Shim, L.-M. Song, N. E. Marcon, B. C. Wilson, In vivo near-infrared Raman spectroscopy: Demonstration of feasibility during clinical gastrointestinal endoscopy. *Photochem. Photobiol.* **72**, 146–150 (2000).
21. M. Boncheva, J. de Sterke, P. J. Caspers, G. J. Puppels, Depth profiling of *Stratum corneum* hydration in vivo: A comparison between conductance and confocal Raman spectroscopic measurements. *Exp. Dermatol.* **18**, 870–876 (2009).
22. A. Mahadevan-Jansen, M. F. Mitchell, N. Ramanujam, U. Utzinger, R. Richards-Kortum, Development of a fiber optic probe to measure NIR Raman spectra of cervical tissue in vivo. *Photochem. Photobiol.* **68**, 427–431 (1998).
23. R. O. P. Draga, M. C. M. Grimbergen, P. L. M. Vijverberg, C. F. P. van Swol, T. G. N. Jonges, J. A. Kummer, J. L. H. Ruud Bosch, In vivo bladder cancer diagnosis by high-volume Raman spectroscopy. *Anal. Chem.* **82**, 5993–5999 (2010).
24. A. Mizuno, H. Kitajima, K. Kawauchi, S. Muraishi, Y. Ozaki, Near-infrared Fourier transform Raman spectroscopic study of human brain tissues and tumours. *J. Raman Spectrosc.* **25**, 25–29 (1994).
25. A. Mizuno, T. Hayashi, K. Tashibu, S. Maraishi, K. Kawauchi, Y. Ozaki, Near-infrared FT-Raman spectra of the rat brain tissues. *Neurosci. Lett.* **141**, 47–52 (1992).
26. A. Beljebbar, S. Dukic, N. Amharref, M. Manfait, Ex vivo and in vivo diagnosis of C6 glioblastoma development by Raman spectroscopy coupled to a microprobe. *Anal. Bioanal. Chem.* **398**, 477–487 (2010).
27. S. N. Kalkanis, R. E. Kast, M. L. Rosenblum, T. Mikkelsen, S. M. Yurgelevic, K. M. Nelson, A. Raghunathan, L. M. Poisson, G. W. Auner, Raman spectroscopy to distinguish grey matter, necrosis, and glioblastoma multiforme in frozen tissue sections. *J. Neurooncol.* **116**, 477–485 (2014).
28. S. Koljenović, L.-P. Choo-Smith, T. C. Bakker Schut, J. M. Kros, H. J. van den Berge, G. J. Puppels, Discriminating vital tumor from necrotic tissue in human glioblastoma tissue samples by Raman spectroscopy. *Lab. Invest.* **82**, 1265–1277 (2002).
29. M. Ji, D. A. Orringer, C. W. Freudiger, S. Ramkissoon, X. Liu, D. Lau, A. J. Golby, I. Norton, M. Hayashi, N. Y. R. Agar, G. S. Young, C. Spino, S. Santagata, S. Camelo-Piragua, K. L. Ligon, O. Sagher, X. S. Xie, Rapid, label-free detection of brain tumors with stimulated Raman scattering microscopy. *Sci. Transl. Med.* **5**, 201ra119 (2013).
30. Q. Fang, Mesh-based Monte Carlo method using fast ray-tracing in Plücker coordinates. *Biomed. Opt. Express* **1**, 165–175 (2010).
31. Q. Fang, D. R. Kaeli, Accelerating mesh-based Monte Carlo method on modern CPU architectures. *Biomed. Opt. Express* **3**, 3223–3230 (2012).
32. T. Meyer, N. Bergner, C. Bielecki, C. Krafft, D. Akimov, B. F. M. Romeike, R. Reichart, R. Kalff, B. Dietzek, J. Popp, Nonlinear microscopy, infrared, and Raman microspectroscopy for brain tumor analysis. *J. Biomed. Opt.* **16**, 021113 (2011).
33. J. H. Friedman, Stochastic gradient boosting. *Comput. Stat. Data Anal.* **38**, 367–378 (2002).
34. M. S. Berger, A. V. Deliganis, J. Dobbins, G. E. Keles, The effect of extent of resection on recurrence in patients with low grade cerebral hemisphere gliomas. *Cancer* **74**, 1784–1791 (1994).
35. G. E. Keles, K. R. Lamborn, M. S. Berger, Low-grade hemispheric gliomas in adults: A critical review of extent of resection as a factor influencing outcome. *J. Neurosurg.* **95**, 735–745 (2001).
36. C. Leighton, B. Fisher, G. Bauman, S. Depiero, L. Stitt, D. MacDonald, G. Cairncross, Supratentorial low-grade glioma in adults: An analysis of prognostic factors and timing of radiation. *J. Clin. Oncol.* **15**, 1294–1301 (1997).
37. J. S. Smith, E. F. Chang, K. R. Lamborn, S. M. Chang, M. D. Prados, S. Cha, T. Tihan, S. Vandenberg, M. W. McDermott, M. S. Berger, Role of extent of resection in the long-term outcome of low-grade hemispheric gliomas. *J. Clin. Oncol.* **26**, 1338–1345 (2008).
38. M. J. McGirt, K. L. Chaichana, F. J. Attenello, J. D. Weingart, K. Than, P. C. Burger, A. Olivi, H. Brem, A. Quinoñes-Hinojosa, Extent of surgical resection is independently associated with survival in patients with hemispheric infiltrating low-grade gliomas. *Neurosurgery* **63**, 700–707; author reply 707–708 (2008).

39. N. Sanai, M.-Y. Polley, M. W. McDermott, A. T. Parsa, M. S. Berger, An extent of resection threshold for newly diagnosed glioblastomas. *J. Neurosurg.* **115**, 3–8 (2011).

40. W. Stummer, H.-J. Reulen, T. Meinel, U. Pichlmeier, W. Schumacher, J.-C. Tonn, V. Rohde, F. Oppel, B. Turowski, C. Woiciechowsky, K. Franz, T. Pietsch; ALA-Glioma Study Group, Extent of resection and survival in glioblastoma multiforme: Identification of and adjustment for bias. *Neurosurgery* **62**, 564–576 (2008).

41. A. Pirzkall, S. J. Nelson, T. R. McKnight, M. M. Takahashi, X. Li, E. E. Graves, L. J. Verhey, W. W. Wara, D. A. Larson, P. K. Sneed, Metabolic imaging of low-grade gliomas with three-dimensional magnetic resonance spectroscopy. *Int. J. Radiat. Oncol. Biol. Phys.* **53**, 1254–1264 (2002).

42. R. A. Cairns, T. W. Mak, Oncogenic isocitrate dehydrogenase mutations: Mechanisms, models, and clinical opportunities. *Cancer Discov.* **3**, 730–741 (2013).

43. J. Zhao, H. Lui, D. I. McLean, H. Zeng, Automated autofluorescence background subtraction algorithm for biomedical Raman spectroscopy. *Appl. Spectrosc.* **61**, 1225–1232 (2007).

44. D. G. Leslie, R. E. Kast, J. M. Poulik, R. Rabah, S. Sood, G. W. Auner, M. D. Klein, Identification of pediatric brain neoplasms using Raman spectroscopy. *Pediatr. Neurosurg.* **48**, 109–117 (2012).

45. R. Caruana, A. Niculescu-Mizil, in *Proceedings of the 23rd International Conference on Machine Learning* (Association for Computing Machinery, New York, 2006), pp. 161–168.

46. E. Bauer, R. Kohavi, An empirical comparison of voting classification algorithms: Bagging, boosting, and variants. *Mach. Learn.* **36**, 105–139 (1999).

47. D. N. Louis, H. Ohgaki, O. D. Wiestler, W. K. Cavenee, P. C. Burger, A. Jouvet, B. W. Scheithauer, P. Kleihues, The 2007 WHO classification of tumours of the central nervous system. *Acta Neuropathol.* **114**, 97–109 (2007).

Editor's Summary

Probing for brain tumors

Gliomas are invasive cancers, spreading quietly throughout the brain. They pose a formidable challenge to surgeons who try to remove all cancer cells during resection; leaving any cancer behind can lower the patient's prospects for survival. Jermyn *et al.* adapted Raman spectroscopy for the operating room by developing an imaging technique that uses a commercially available, handheld contact fiber optic probe. The probe's optic cables were connected to a near-infrared laser, for stimulating tissue molecules; in turn, these components were linked to a computer to visualize resulting spectra in real time. When held against human brain tissue, the probe measured the Raman scattering signal, which was separated from background signals and differentiated from "normal" tissues using certain algorithms. The authors tested the probe in 17 patients with grade 2 to 4 gliomas who were undergoing surgery and compared imaging results with 161 biopsy samples. Intraoperative Raman imaging allowed the authors to detect both invasive and dense cancer cells with an accuracy of 92%. By comparison, the surgeon, using standard surgical tools like the bright-field microscope and magnetic resonance imaging, identified cancer with 73% accuracy. Such label-free, portable, intraoperative imaging technologies will be important in improving the efficiency of tumor resections and, in turn, for extending survival times of glioma patients.

A complete electronic version of this article and other services, including high-resolution figures, can be found at:
http://stm.sciencemag.org/content/7/274/274ra19.full.html

Supplementary Material can be found in the online version of this article at:
http://stm.sciencemag.org/content/suppl/2015/02/09/7.274.274ra19.DC1.html

Related Resources for this article can be found online at:
http://stm.sciencemag.org/content/scitransmed/5/201/201ra119.full.html
http://stm.sciencemag.org/content/scitransmed/7/271/271ra7.full.html
http://stm.sciencemag.org/content/scitransmed/5/194/194ra93.full.html
http://stm.sciencemag.org/content/scitransmed/5/216/216rv4.full.html
http://stm.sciencemag.org/content/scitransmed/3/71/71ra15.full.html
http://stm.sciencemag.org/content/scitransmed/3/79/79ra33.full.html

Information about obtaining **reprints** of this article or about obtaining **permission to reproduce this article** in whole or in part can be found at:
http://www.sciencemag.org/about/permissions.dtl